Wave propagation in beams with periodic arrays of airfoil-shaped resonating units

Filippo Casadei [a], Katia Bertoldi [a,b,*]

[a] School of Engineering and Applied Sciences, Harvard University, Cambridge, MA 02138, United States
[b] Kavli Institute for Bionano Science, Harvard University, Cambridge, MA 02138, United States

ARTICLE INFO

ABSTRACT

This paper presents an analytical and numerical study on the dispersion properties of an Euler–Bernoulli beam immersed in a steady fluid flow with periodic arrays of airfoil-shaped vibration absorbers attached to it. The resonance characteristics of the airfoils generate strong attenuation of flexural waves in the beam occurring at frequencies defined by the properties of the airfoils and the speed of the incident fluid. Analytical and numerical tools are developed to investigate the effects of the incident flow on the dispersion properties and the bandgaps of the system. Both steady and unsteady aerodynamic models are used to model the lift force and the pitching moment acting on the resonators and their effect on the dispersion relations of the system is evaluated. Finally, an effective medium description of the beam is developed to capture its behavior at long-wavelengths. In this regime, the system can be effectively considered as an acoustic metamaterial with adaptive dispersion properties.

1. Introduction

The problem of wave propagation in periodic structures is receiving increasing attention because of the ability of these systems to effectively filter elastic waves [1]. This is commonly achieved through the generation of bandgaps (or stop bands) – frequency ranges of strong wave attenuation - which can be formed either by Bragg scattering [2–4] at high impedance mismatch zones, or by introducing resonating units in a host structure [5–7]. While Bragg-type bandgaps typically occur at wavelengths of the order of the unit cell size [8,2], locally resonant bandgaps arise in the vicinity of the natural frequency of the resonating units [5] and are modestly affected by the spatial periodicity of the system. Because of this interesting property, locally resonant structures have been proposed as acoustic barriers [9,10], vibration isolators [11] and noise suppression devices [12,13] with particular emphasis on low frequency applications [14].

Motivated by all these applications, the response of structural elements such as rods [15,16], beams [17–19], and plates/shells [20–22] with arrays of spring–mass resonators with single [23–25] or multiple [26–28] degrees of freedom has been studied both numerically and experimentally [29], showing that remarkable wave attenuation characteristics can be achieved. However, most of the configurations proposed so far operate at fixed frequency ranges and it is often impractical, if not impossible, to tune and control their bandgaps after the assembly of the system.

---

* Corresponding author at: School of Engineering and Applied Sciences, Harvard University, Cambridge, MA 02138, United States.
  E-mail address: bertoldi@seas.harvard.edu (K. Bertoldi).

In an effort to design tunable materials, it has been shown that locally resonant bandgaps can be controlled using either the applied deformation [46] or electro-mechanical resonators consisting of resistive-inductive shunted piezoelectric patches [20,30,31] bonded to a host structure. Moreover, it has been recently demonstrated both experimentally and numerically that fluid–structure interactions can also be exploited to design systems capable of self-regulating their dynamic response [32]. In fact, an elastic structure with a periodic array of airfoil-type mechanical resonators is characterized by bandgaps at frequencies determined by the resonances of the airfoils. Interestingly, when an air flow impinges on the airfoils, the resonators behave as aeroelastic systems subjected to modal convergence [33], so that their resonance frequencies – and consequently the corresponding bandgaps of the primary structure – shift as a function of the fluid speed.

The main purpose of this paper is to expand on the previous investigation [32] by presenting a detailed analytical and numerical study on the influence of the fluid speed on the dispersion properties and bandgaps of a beam with a periodic array of airfoil-shaped resonating units bonded along its length. Both steady and unsteady aerodynamic models are used to describe the fluid-coupled dynamic response of the resonators, as detailed in Section 2. The response of the airfoils and the elastic beam is then coupled in Section 3, yielding a simple formulation which enables us to investigate analytically the propagation of elastic waves in the system as a function of the flow speed. The results of this analysis are presented in Section 4, where the effect of various parameters defining the system on the dispersion properties of the beam is evaluated. Finally, in Section 5 an effective medium description of the beam is developed to capture its behavior at long-wavelengths. This study demonstrates how the proposed concept can be utilized to affect and tune the equivalent mechanical properties of the beam, which can be considered as an example of an adaptive metamaterial.

2. Fluid-coupled dynamic response of the resonator

In this study we consider an Euler–Bernoulli beam with a periodic array of resonating units (vibration absorbers) attached along its length (see Fig. 1a). Each resonator consists of a rigid airfoil-shaped mass m_a (with polar moment of inertia I_a), supported by a linear and torsional spring with stiffness k_h and k_θ respectively (see Fig. 1b). The airfoil is symmetric with respect to its chord (of length $2b$) and characterized by a static unbalance $x_\theta \equiv e - a$, where a and e are dimensionless parameters that define the location of the pivoting point and center of gravity, respectively (see Fig. 1b).

An incompressible and inviscid fluid flow impinges on the system with an asymptotic speed V_∞. The aerodynamic loads generated by the flow on the surface of the airfoils are described in terms of a concentrated lift force ($\mathcal{L}$) and moment ($\mathcal{M}$), as shown in Fig. 1b. Note that in our analysis (i) because of its small thickness and width, we neglect the effect of the fluid on the response of the beam, and (ii) for the sake of simplicity, we do not consider any aerodynamic interactions between adjacent airfoils.

We start by deriving the equations governing the dynamic behavior of the resonating unit shown in Fig. 1b, which can be written as

$$\widehat{\mathbf{M}}\ddot{\mathbf{q}} + \widehat{\mathbf{K}}\mathbf{q} = \widehat{\mathbf{r}} \tag{1}$$
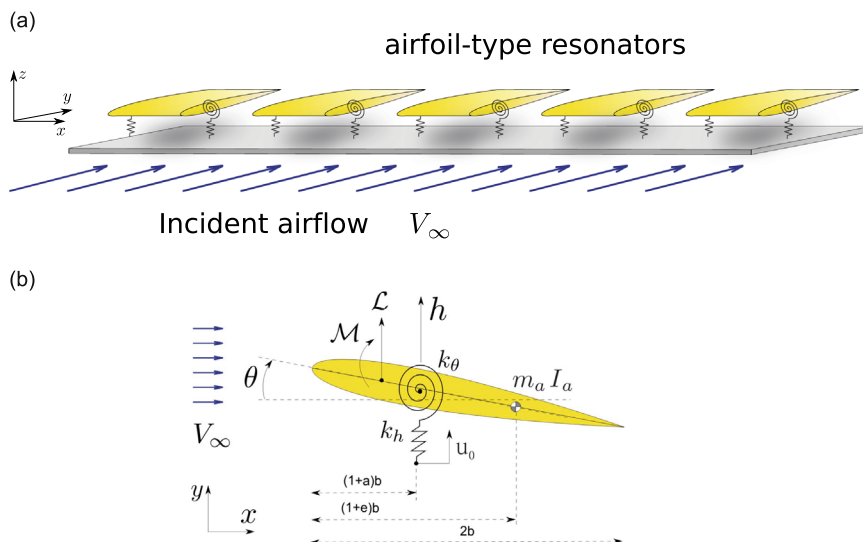

Fig. 1. (a) Beam with periodic array of airfoil-shaped resonators attached to it. (b) Details of the airfoil-shaped vibration absorber (side view).

where

$$\widehat{\mathbf{K}} = \begin{bmatrix} k_\theta & 0 & 0 \\ 0 & k_h & -k_h \\ 0 & -k_h & k_h \end{bmatrix} \quad \text{and} \quad \widehat{\mathbf{M}} = \begin{bmatrix} I_a & -m_a b x_\theta & 0 \\ -m_a b x_\theta & m_a & 0 \\ 0 & 0 & 0 \end{bmatrix}, \tag{2}$$

are the mass and stiffness matrices of the system, and

$$\mathbf{q} = [\theta, \ h, \ u_0]^T, \quad \widehat{\mathbf{r}} = [\mathcal{M} + b(1/2+a)\mathcal{L}, \ \mathcal{L}, \ f_0]^T \tag{3}$$

are vectors containing the degrees of freedom of the system and external loads acting on the airfoil, respectively. In the above, θ and h denote the pitch and plunge degrees of freedom of the airfoil, u_0 is the displacement of the point attached to the beam and f_0 is the reaction force transmitted from the beam.

Here, the aerodynamic lift force $\mathcal{L}$ and the pitching moment $\mathcal{M}$ acting on the resonator are modeled using both steady and unsteady flow theories [34,35]. While the former provides a simpler representation of the aerodynamic loads and enables us to derive closed-form expressions of dispersion relations and effective properties, unsteady flow models, such as the one proposed by Peters et al. [35], need to be used when the characteristic time of oscillation of the airfoil is comparable to the time a fluid particle interacts with the airfoil [34].

Regardless of the specific adopted aerodynamic model, by substituting the expressions for $\mathcal{L}$ and $\mathcal{M}$ into Eq. (1) the dynamic equations of motion of the resonator can be recast as

$$\mathbf{M}\ddot{\mathbf{q}} + \mathbf{C}\dot{\mathbf{q}} + \mathbf{K}\mathbf{q} = \mathbf{r}, \tag{4}$$

where $\mathbf{r} = [0, \ 0, \ f_0]^T$ and the explicit expressions for $\mathbf{M}$, $\mathbf{C}$, and $\mathbf{K}$ depend on the specific aerodynamic theory being used.

Furthermore, assuming harmonic motion at frequency ω (i.e. $\mathbf{q} = \mathbf{q}_0 e^{i\omega t}$, and $\mathbf{r} = \mathbf{r}_0 e^{i\omega t}$, $i = \sqrt{-1}$ being the imaginary unit) Eq. (4) can be rewritten as

$$(\mathbf{K} + i\omega \mathbf{C} - \omega^2 \mathbf{M})\mathbf{q}_0 = \mathbf{r}_0, \tag{5}$$

which can be dynamically condensed, yielding

$$u_0 = D_0(\omega, V_\infty) f_0, \tag{6}$$

$D_0(\omega, V_\infty)$ denoting the condensed dynamic stiffness of the resonator, which in Section 3 will be used to explicitly derive the dispersion relations for a beam with an array of fluid-coupled resonators.

2.1. Steady aerodynamic model

Assuming a steady-flow aerodynamic approximation, the external loads acting on a symmetric airfoil-shaped mass can be expressed as [34]

$$\mathcal{L} = 2\pi b \rho_\infty V_\infty^2 \theta$$
$$\mathcal{M} = 0 \tag{7}$$

Substituting Eq. (7) into Eq. (1), the dynamic equations governing the response of the resonator can be recast as in Eq. (4) with $\mathbf{M} = \widehat{\mathbf{M}}$, $\mathbf{C} = \mathbf{0}$, and $\mathbf{K} = \widehat{\mathbf{K}} - \mathbf{K}_{am}$, $\mathbf{K}_{am}$ denoting the flow-induced stiffness term [34]

$$\mathbf{K}_{am} = 2\pi b \rho_\infty V_\infty^2 \begin{bmatrix} (1/2+a)b & 0 & 0 \\ 1 & 0 & 0 \\ 0 & 0 & 0 \end{bmatrix}. \tag{8}$$

Despite its simplicity this aerodynamic model captures the aeroelastic coupling between the airfoil and the fluid flow, since the effective stiffness matrix $\mathbf{K}$ is a function of the incident fluid speed (V_∞). Using this aerodynamic model a closed-form expression for D_0 in Eq. (6) can also be obtained

$$\frac{D_0}{k_h} = 1 - \frac{1}{1 - \zeta^2 + \frac{b x_\theta \zeta^2 (b k_h x_\theta \zeta^2 - 2\pi b \rho_\infty V_\infty^2)}{2\pi \rho_\infty (a+1/2)b^2 V_\infty^2 + I_a \omega_h^2 \zeta^2 - k_\theta}}, \tag{9}$$

in which the following non-dimensional parameters have been introduced

$$\zeta \equiv \frac{\omega}{\omega_h} \quad \text{and} \quad \omega_h \equiv \sqrt{k_h / m_a}. \tag{10}$$

2.2. Quasi-steady aerodynamic model

To capture the effect of the motion of the airfoil on the relative wind direction and the time dependence of the angle of attack without compromising on the simplicity of the formulation, we then consider a quasi-steady aerodynamic

model [34], so that

$$\mathcal{L} = 2\pi b \rho_\infty V_\infty^2 \left(\theta + \frac{\dot{h}}{V_\infty} \right)$$
$$\mathcal{M} = -\pi b^3 \rho_\infty V_\infty \dot{\theta} \tag{11}$$

where the second term in the lift equation accounts for the variation of the angle of attack along the chord-wise direction and provides damping to the plunge motion. Substitution of Eqs. (11) into Eq. (1) yields Eq. (4) with $\mathbf{M} = \widehat{\mathbf{M}}$, $\mathbf{C} = -\mathbf{C}_{am}$, and $\mathbf{K} = \widehat{\mathbf{K}} - \mathbf{K}_{am}$, where $\mathbf{K}_{am}$ is given in Eq. (8) and

$$\mathbf{C}_{am} = 2\pi b \rho_\infty V_\infty \begin{bmatrix} -b^2/2 & -(1/2+a)b & 0 \\ 0 & -1 & 0 \\ 0 & 0 & 0 \end{bmatrix}. \tag{12}$$

2.3. Unsteady aerodynamic model

A more realistic description of the unsteady effects associated with the oscillatory motion of the airfoil is provided by the finite-state, induced-flow theory for inviscid, incompressible flow of Peters et al. [35]. According to this model the lift force and the pitching moment are given by

$$\mathcal{L} = \pi \rho_\infty b^2 \left(\ddot{h} + V_\infty \dot{\theta} - ba\ddot{\theta} \right) + 2\pi \rho_\infty V_\infty b \left[\dot{h} + V_\infty \theta + b\left(\frac{1}{2} - a \right)\dot{\theta} - \frac{1}{2}\mathbf{b}^T \lambda \right],$$

$$\mathcal{M} = -\pi \rho_\infty b^3 \left[\frac{1}{2}\ddot{h} + V_\infty \dot{\theta} + b\left(\frac{1}{8} - \frac{a}{2} \right)\ddot{\theta} \right], \tag{13}$$

where ρ_∞ is the free stream air density, and λ is a vector containing the N_p induced flow terms λ_n ($n = 1, \ldots, N_p$). Note that $N_p = 6$ has been used in this study, since a higher number of induced flow terms did not appreciably alter the results. The evolution of the state vector λ is expressed in terms of N_p first-order ordinary differential equations as

$$\mathbf{A}\dot{\lambda} + \frac{V_\infty}{b}\lambda = \mathbf{c}\left[\ddot{h} + V_\infty \dot{\theta} + b\left(\frac{1}{2} - a \right)\ddot{\theta} \right], \tag{14}$$

where $\mathbf{A}$, $\mathbf{b}$ and $\mathbf{c}$ denote arrays of known coefficients reported in Appendix A. Although in this case the system has $3 + N_p$ degrees of freedom, by substituting Eqs. (13) into Eq. (1) and by adding Eq. (14) the dynamics of the airfoil can still be recast as in Eq. (4) with $\mathbf{q} = [\theta,\ h,\ u_0,\ \lambda]^T$, $\mathbf{r} = [0,\ 0,\ f_0,\ \mathbf{0}]^T$, and

$$\mathbf{K} = \begin{bmatrix} \widehat{\mathbf{K}} - \mathbf{K}_{am} & -\mathbf{h}_{am} \\ \mathbf{0} & \frac{V_\infty}{b}\mathbf{I}_{N_p} \end{bmatrix}, \quad \mathbf{C} = \begin{bmatrix} -\tilde{\mathbf{C}}_{am} & \mathbf{0} \\ -\boldsymbol{\beta} & \mathbf{A} \end{bmatrix}, \quad \mathbf{M} = \begin{bmatrix} \widehat{\mathbf{M}} - \mathbf{M}_{am} & \mathbf{0} \\ \boldsymbol{\alpha} & \mathbf{0} \end{bmatrix}, \tag{15}$$

where $\mathbf{K}_{am}$ is given in Eq. (8) and

$$\tilde{\mathbf{C}}_{am} = 2\pi b \rho_\infty V_\infty \begin{bmatrix} ab^2(1-2a)/2 & -(1/2+a)b & 0 \\ b(1-a) & -1 & 0 \\ 0 & 0 & 0 \end{bmatrix},$$

$$\mathbf{M}_{am} = \pi b^2 \rho_\infty \begin{bmatrix} -b^2(a^2+1/8) & -ab & 0 \\ -ab & -1 & 0 \\ 0 & 0 & 0 \end{bmatrix},$$

$$\mathbf{h}_{am} = 2\pi b \rho_\infty V_\infty [-b(1/2+a)\mathbf{b}^T,\ -\mathbf{b}^T,\ \mathbf{0}]^T,$$

$$\boldsymbol{\alpha} = -\mathbf{c}[b(1/2-a),\ 1,\ 0]^T, \quad \text{and}$$

$$\boldsymbol{\beta} = V_\infty \mathbf{c}[1,\ 0,\ 0]^T. \tag{16}$$

3. Wave propagation in an infinite beam with airfoil resonators

The aeroelastic behavior of the airfoil-shaped vibration absorbers described in the previous section is exploited here to alter the dispersion relations and the bandgaps of an Euler–Bernoulli beam characterized by bending stiffness EI and mass per unit length ρA with a periodic array of such resonators uniformly distributed along its length. In particular, we focus on

an infinitely long beam, consider a unit cell of length L (see Fig. 2a) and investigate the propagation of elastic waves using the Euler–Bernoulli spectral stiffness matrix [36] and the transfer matrix approach [1,37].

Denoting by $\mathbf{u}_L = [w_L\ \theta_L]$ and $\mathbf{u}_R = [w_R\ \theta_R]$ the generalized displacements at the left (L) and right (R) boundaries of the cell (see Fig. 2b), the dynamic response of the system can be described as

$$\mathbf{K}_D(\omega)\mathbf{u}(\omega) = \mathbf{f}(\omega), \tag{17}$$

where $\mathbf{u} = [\mathbf{u}_L,\ \mathbf{u}_R]^T$ is a vector of generalized displacements at the two ends of the beam, and $\mathbf{f} = [\mathbf{f}_L,\ \mathbf{f}_R]^T$ is the corresponding vector of external loads. In Eq. (17), the dynamic stiffness matrix of the beam is given by [18]

$$\mathbf{K}_D = \begin{bmatrix} \mathbf{K}_{11} & \mathbf{K}_{12} \\ \mathbf{K}_{21} & \mathbf{K}_{22} \end{bmatrix}, \tag{18}$$

where the sub-matrices $\mathbf{K}_{ij}$ $(i,j = 1,2)$ are defined as

$$\mathbf{K}_{11} = \frac{EI}{L^3} \begin{bmatrix} a_1 & c_2 L \\ c_2 L & b_1 L^2 \end{bmatrix},$$

$$\mathbf{K}_{12} = \mathbf{K}_{21}^T = \frac{EI}{L^3} \begin{bmatrix} -a_2 & c_1 L \\ -c_1 L & b_2 L^2 \end{bmatrix},$$

$$\mathbf{K}_2 = \frac{EI}{L^3} \begin{bmatrix} a_1 & -c_2 L \\ -c_2 L & b_1 L^2 \end{bmatrix}. \tag{19}$$

and

$$a_1 = \left[\sin \kappa_b L \cosh \kappa_b L + \cos \kappa_b L \sinh \kappa_b L \right] \frac{(\kappa_b L)^3}{\Delta},$$

$$a_2 = \left[\sinh \kappa_b L + \sin \kappa_b L \right] \frac{(\kappa_b L)^3}{\Delta},$$

$$b_1 = \left[\sin \kappa_b L \cosh \kappa_b L - \cos \kappa_b L \sinh \kappa_b L \right] \frac{\kappa_b L}{\Delta},$$

$$b_2 = \left[\sinh \kappa_b L - \sin \kappa_b L \right] \frac{\kappa_b L}{\Delta},$$

$$c_1 = \left[\cosh \kappa_b L - \cos \kappa_b L \right] \frac{(\kappa_b L)^2}{\Delta},$$

$$c_2 = \sinh \kappa_b L \sin \kappa_b L \frac{(\kappa_b L)^2}{\Delta},$$

$$\Delta = 1 - \cosh \kappa_b L \cos \kappa_b L, \tag{20}$$

$\kappa_b = [\rho A \omega^2/(EI)]^{1/4}$ denoting the wavenumber of flexural waves propagating in the beam [36].

The dynamic equations of motion of the unit cell comprising both the beam and the airfoil-type resonator attached to its left end (Fig. 2) can then be obtained as

$$\mathbf{D}(\omega)\mathbf{u} = \mathbf{f}, \tag{21}$$
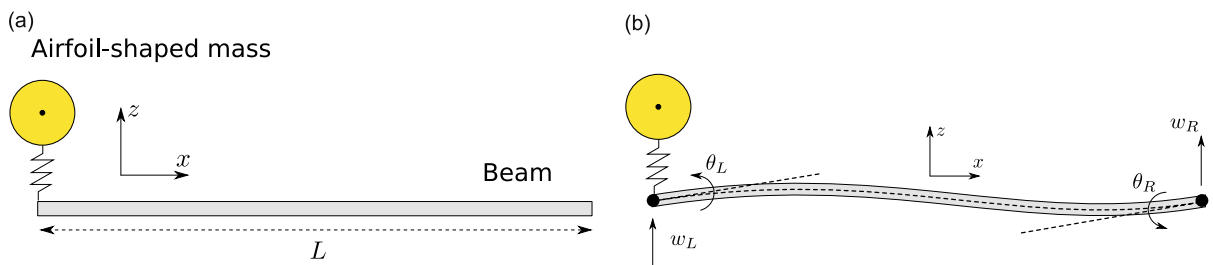

Fig. 2. (a) Front view of the undeformed unit cell comprising a portion of the beam (of length L) and an airfoil resonator attached to its left end. (b) Front view of the deformed unit cell showing the degrees of freedom used in the analysis.

where

$$\mathbf{D} = \begin{bmatrix} \mathbf{D}_{LL} & \mathbf{D}_{LR} \\ \mathbf{D}_{RL} & \mathbf{D}_{RR} \end{bmatrix} = \begin{bmatrix} \mathbf{K}_{11} + \mathbf{D}_0 & \mathbf{K}_{12} \\ \mathbf{K}_{21} & \mathbf{K}_{22} \end{bmatrix}, \tag{22}$$

and

$$\mathbf{D}_0 = \begin{bmatrix} D_0(\omega, V_\infty) & 0 \\ 0 & 0 \end{bmatrix}, \tag{23}$$

with D_0 denoting the dynamic stiffness of the resonator defined in Eq. (6).

Wave propagation in the infinite periodic system is investigated by imposing Bloch periodic boundary conditions [38,39] at the left (L) and right (R) ends of the cell

$$\mathbf{u}_R = e^\mu \mathbf{u}_L, \quad \text{and} \quad \mathbf{f}_R = -e^\mu \mathbf{f}_L, \tag{24}$$

where $\mu(\omega)$ is the complex propagation constant. Substitution of Eqs. (24) into Eq. (21) yields the well-known quadratic eigenvalue problem [18]

$$[\mathbf{D}_{RL} + (\mathbf{D}_{LL} + \mathbf{D}_{RR})e^\mu + \mathbf{D}_{LR}e^{2\mu}]\mathbf{u}_L = \mathbf{0}, \tag{25}$$

from which two pairs of propagation constants $\pm\mu_1$ and $\pm\mu_2$ can be calculated, each pair representing waves traveling in opposite directions. While the real part of μ, known as attenuation constant, represents the amplitude decay rate that the wave experiences as it propagates from one cell to the next, the imaginary part of μ, known as phase constant, relates the phase change of a wave at the two ends of the unit cell. Therefore, wave propagation is possible within frequency bands where either μ_1 or μ_2 is purely imaginary (i.e. $\text{Real}(\mu_1) = 0$ or $\text{Real}(\mu_2) = 0$), while bandgaps occur at frequencies characterized by non-zero attenuation constants (i.e. $\text{Real}(\mu_1) \neq 0$ and $\text{Real}(\mu_2) \neq 0$).

4. Results and discussion

We now show how the aeroelastic behavior of the considered resonating units affects the dispersion properties of the system. In this study we consider a configuration defined by the following set of non-dimensional parameters:

$$\ell = \frac{L}{b} = 4.5, \quad \psi = \frac{M_{\text{beam}}}{m_a} = 2, \quad \delta = \frac{\text{EI}}{L^3 k_h} = 20,$$

$$r^2 = \frac{I_a}{m_a b^2} = 1.3, \quad \sigma = \frac{\omega_h}{\omega_\theta} = 1.1, \quad U = \frac{V_\infty}{b\omega_\theta}, \tag{26}$$

where $\omega_h = \sqrt{k_h/m_a}$ and $\omega_\theta = \sqrt{k_\theta/I_a}$ are the uncoupled natural frequencies of the airfoils at zero airspeed, $M_{\text{beam}} = \rho AL$ is the beam mass, and U represents a non-dimensional flow speed parameter.

4.1. Aeroelastic response of the resonator

We start by considering an airfoil resonator with the plunge spring (k_h) rigidly connected to the ground (i.e. $u_0 = 0$). The aeroelastic response is investigated by solving Eq. (5) for the complex natural frequencies of the system (ω_n) by setting the right hand side term to zero [34]. In Fig. 3 we report the variation of the imaginary ($\Omega = \text{Imag}(\omega_n)$) and real ($\Gamma = \text{Real}(\omega_n)$) part of the natural frequencies of the airfoil as a function of the flow speed parameter (U) obtained using the three aerodynamic models previously introduced. As expected, the results reveal that the pitch frequency monotonically increases for increasing values of U, while the opposite trend is observed for the frequency associated with the heave (plunge) mode. Moreover, after a critical value of the speed parameter, commonly known as flutter speed (U_f), the real part of the natural frequency associated with the pitch mode becomes positive indicating the onset of a dynamic instability. Above this critical speed U_f the dynamics of the system becomes highly nonlinear [40] and the study of this regime falls outside the scope of the present investigation.

Results reported in Fig. 3 also show that all three aerodynamic models considered in this study provide similar predictions for the variation of the natural frequency of the airfoils as a function of the flow speed. In particular, the agreement between the three models is excellent at low speeds, while their different aerodynamic damping terms lead to slightly different values of flutter speed U_f and frequency Ω_f, as shown in Table 1.

To further gain insights into the aeroelastic behavior of the resonating unit, the steady aerodynamic model is exploited to investigate the variation of the flutter speed U_f and frequency Ω_f for different values of parameters. In particular, we focus on the non-dimensional mass ratio $\psi = M_{\text{beam}}/m_a$, inertia ratio $r^2 = I_a/m_a b^2$ and the airfoil frequency ratio $\sigma = \omega_h/\omega_\theta$, which have been identified as the most relevant parameters governing the aeroelastic response of the airfoils. In Fig. 4a we report the evolution of both U_f and Ω_f as a function of ψ. The results indicate that for increasing values of ψ – obtained by reducing the mass of the airfoil m_a – U_f is significantly reduced, while Ω_f remains unaltered. Since the flutter instability defines an upper limit for the operation of the proposed device, this suggests that lighter resonators are best suited for low
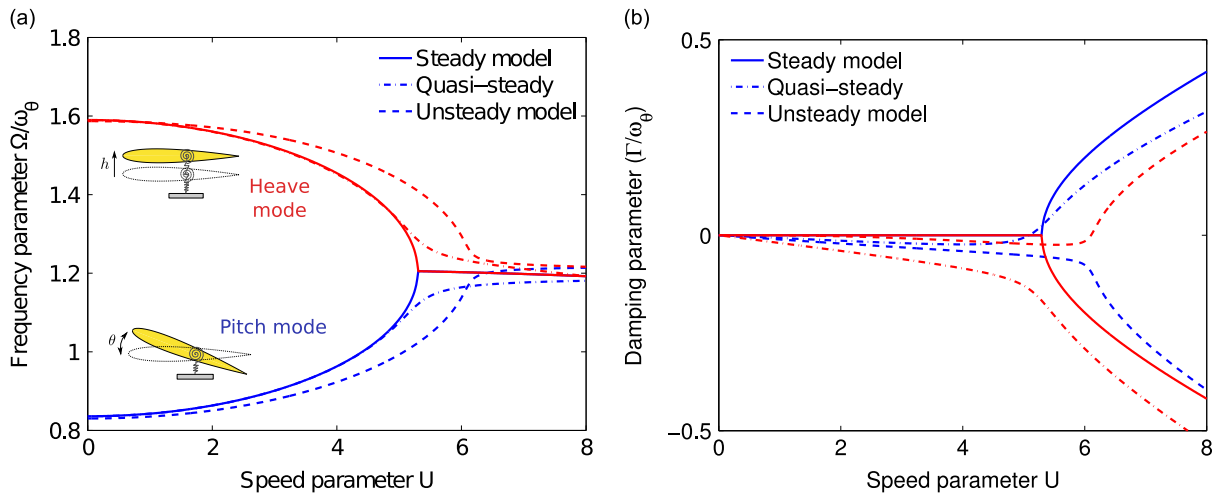
Fig. 3. Effect of the flow speed U on the pitch (blue) and plunge (red) resonance frequencies of the airfoils. (a) Imaginary part of the natural frequencies, $\Omega = \text{Imag}(\omega_n)$. (b) Real part of the natural frequencies, $\Gamma = \text{Real}(\omega_n)$. (For interpretation of the references to color in this figure caption, the reader is referred to the web version of this paper.)

Table 1
Flutter speed (U_f) and frequency (Ω_f) predicted by the steady and unsteady aerodynamic models.

	Steady model	Quasi-steady model	Unsteady model
U_f	5.306	5.090	6.100
Ω_f/ω_θ	1.205	1.089	1.167

speed applications. On the other hand, the results reported in Fig. 4b show that higher values of the inertia ratio r^2 lead to a decrease of both U_f and Ω_f. However, the results also indicate that the effect of r^2 on the flutter speed and frequency is less pronounced than that of the mass parameter ψ. Finally, in Fig. 4c we show the effect of the airfoil frequency ratio σ, which characterizes the separation between the pitch and plunge resonance frequencies. As expected, higher values of σ inevitably lead to higher flutter speeds, since it will generally take longer for the two modes to coalesce.

4.2. Dynamic response of a beam with a periodic array of resonators

Next we investigate the effect of the fluid speed on the dynamic response of an elastic beam with a periodic array of airfoil-type resonators uniformly distributed along its length. We compute analytically the dispersion relations using the approach described in Sections 2 and 3 and considering all the three aerodynamic models introduced there. Furthermore, the analytical solutions are compared with numerical results obtained through the finite element (FE) method. For the numerical calculations the main beam is modeled using Euler–Bernoulli beam elements, while the interaction of the flap with the surrounding fluid is described by either the steady or unsteady aerodynamic models described in Section 2. Bloch–Floquet quasi-periodic conditions [38,39] and the transfer matrix approach [37] are then used to calculate the complex propagation constant $\mu(\omega)$ of the system.

4.2.1. Dispersion relations

We start by computing the dispersion relations of the system in the absence of air flow (i.e. $U=0$), so that both the lift force $\mathcal{L}$ and the pitching moment $\mathcal{M}$ vanish. In this case $\mathbf{D}_0 = \mathbf{0}$ in Eq. (23) and the two propagation constants μ_1 and μ_2 can be analytically calculated from Eq. (25). The results are presented in Fig. 5 showing the variation of the phase constants (i.e. $\text{Imag}(\mu_1)$ and $\text{Imag}(\mu_2)$ in Fig. 5a) and attenuation constants (i.e. $\text{Real}(\mu_1)$ and $\text{Real}(\mu_2)$ in Fig. 5b) as a function of the non-dimensional frequency parameter ω/ω_θ. In the figure both analytical (red and blue lines) and FE (circular markers) results are reported, showing an excellent agreement. In Fig. 5a we also include the dispersion relation of a uniform Euler–Bernoulli beam (see black dashed line). While at low frequencies the phase constants of our periodic system closely resemble the dispersion properties of a uniform Euler–Bernoulli beam, the results indicate the presence of two regions of negative group velocity and strong dispersion centered at $\omega/\omega_\theta = 0.76$ and $\omega/\omega_\theta = 1.44$. In these ranges, both wave modes are characterized by positive real part (Fig. 5b), indicating the presence of a bandgap (or stop band) in which waves are strongly
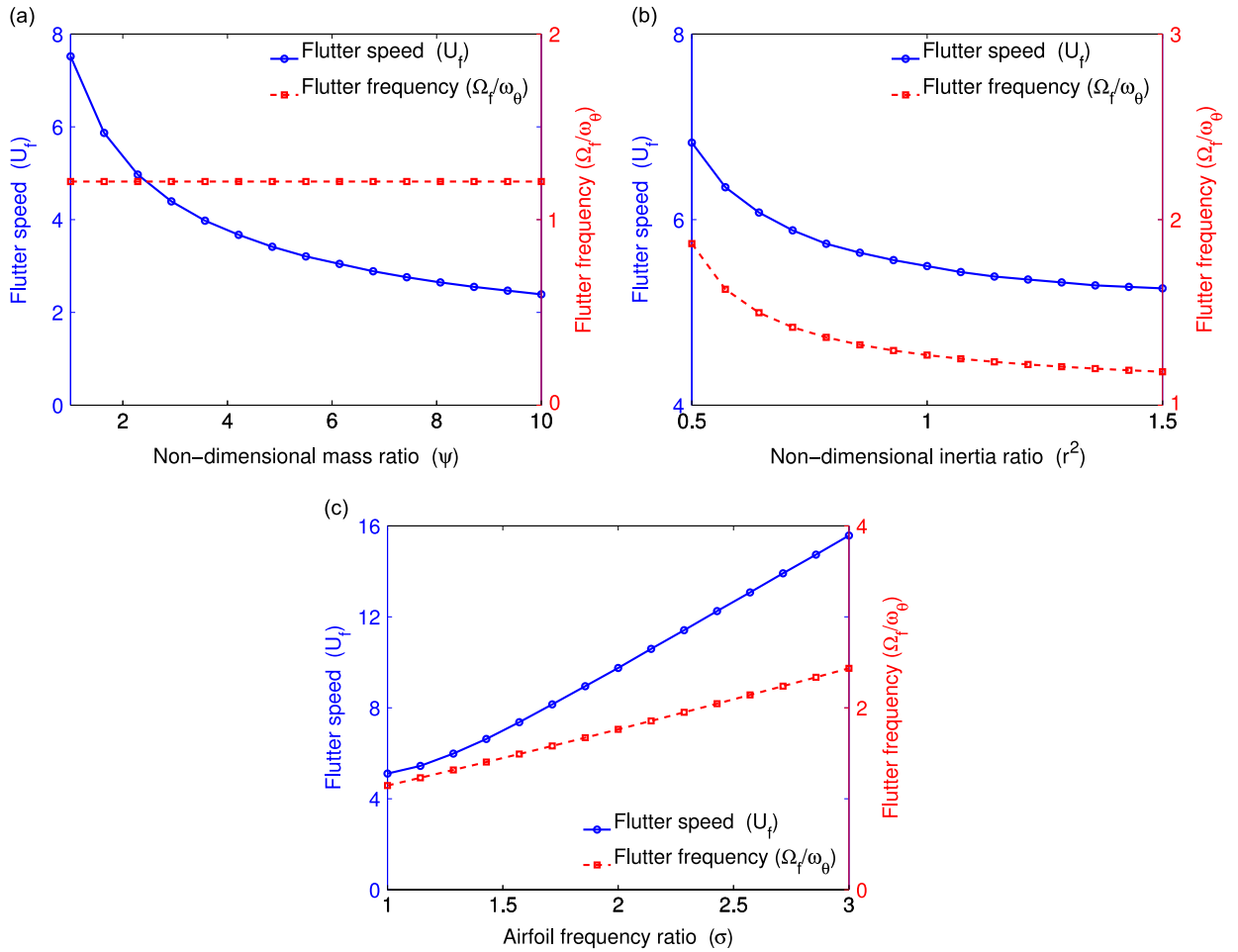
Fig. 4. Effect of (a) the non-dimensional mass ratio ψ, (b) the inertia ratio r^2, and (c) the airfoil frequency ratio σ on the flutter speed U_f and frequency Ω_f/ω_θ.
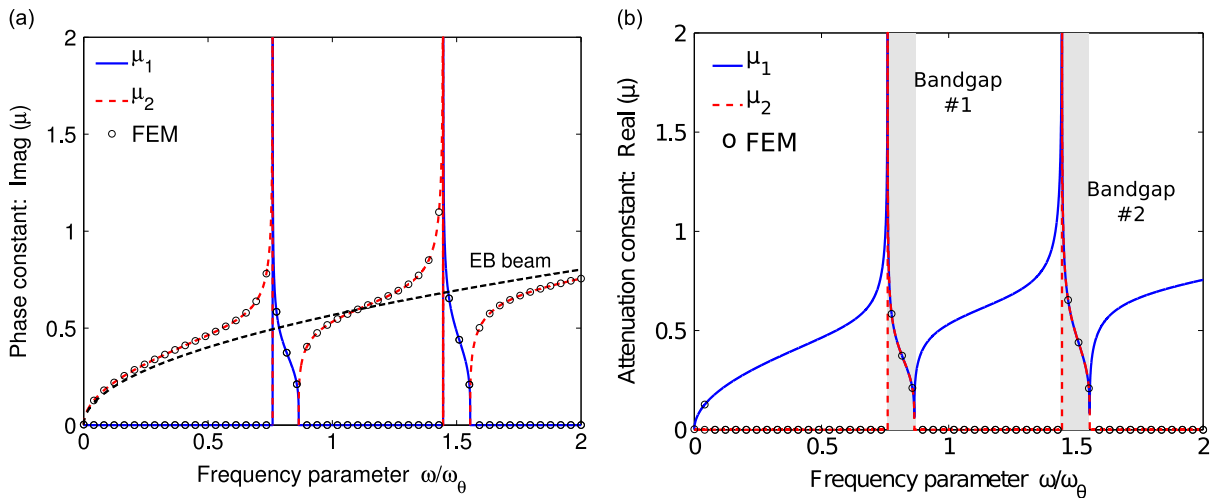

Fig. 5. Dispersion relations of the propagation constants μ_1 (solid blue line), and μ_2 (dashed red line) in the absence of flow ($U=0$). The analytical solution (lines) is compared with the FE results (○ markers) showing excellent agreement. (a) Imaginary part. (b) Real part. (For interpretation of the references to color in this figure caption, the reader is referred to the web version of this paper.)

attenuated. The lower-frequency bandgap (denoted as bandgap #1 in Fig. 5b) is induced by the pitch resonance of the airfoil, while the higher-frequency gap (bandgap #2 in Fig. 5b) is associated with the vertical (plunge) motion of the mass. Finally, it is worth noticing that the bandgaps occur in the vicinity of the pitch and plunge resonance frequencies of the corresponding airfoils shown in Fig. 3a at $U=0$, confirming their locally-resonance nature.

4.2.2. Fluid-coupled dispersion relations

Next, we investigate the effect of the incident fluid on the dispersion properties of the beam, and compare the results obtained using different aerodynamic theories. Since the wave attenuation properties inside the bandgaps are mostly quantified by the smallest attenuation constant of the system $\Xi = \min(\mathrm{Real}(\mu_1), \mathrm{Real}(\mu_2))$, in Fig. 6 we show the evolution of Ξ as a function of ω/ω_θ for different wind speeds using the three aerodynamic models previously introduced.

Results shown in Fig. 6a indicate that for small values of the flow speed ($U=1$) the bandgaps' frequency ranges predicted by the three modes are almost identical. However, while the steady aerodynamic theory predicts sharp and narrow attenuation regions, the attenuation constant peaks predicted by the quasi-steady and unsteady models are slightly wider and smoother. This is attributed to the fact that the quasi-steady and unsteady models account for the presence of aerodynamic damping induced by the relative motion of the airfoil with respect to the fluid. In fact, the presence of energy dissipating elements within the resonating unit is known to generate wider attenuation regions and to reduce the peak amplitude of the attenuation constant [41,30]. For larger values of flow speed we still find a good agreement between the band gaps predicted using the three different aerodynamic models (see results reported in Fig. 6b for $U=4$), although the discrepancies become more accentuated. The results presented in Fig. 6 have also been validated by comparison with FE calculations, showing excellent agreement. For the sake of brevity, the comparison between the analytical and numerical solutions is shown in Appendix B.

Remarkably, the results shown in Fig. 6 also indicate that for increasing values of the wind speed U the two bandgaps' frequencies gradually approach each other. The progressive coalescence of the two bandgaps is associated with the aeroelastic convergence of the two resonance frequencies of the airfoil shown in Fig. 3a [32]. To further explore the coalescence of the two bandgaps, in Fig. 7 we directly compare the dispersion relations of the system for different values of the incident flow speed, $U = 0.0, 4.0, 5.0$ and 5.3. For the sake of simplicity we only present results computed using the steady aerodynamic, but very similar trends are found when using the other two aerodynamic models. The results clearly illustrate the progressive convergence of the two bandgaps, which interestingly merge in a single broad attenuation region centered at $\omega/\omega_\theta \sim 1.1$ when U approaches the flutter limit. Interestingly, Fig. 7 also shows that the complete coalescence of the two bandgaps occurs only at the flutter speed, since two separate bandgaps are observed for flow speeds only slightly below such limit (i.e. $U=5.0$ case in Fig. 7).

To further study the effect of the flow speed on the bandgaps of the system, we calculate the relative bandgaps' size defined as the ratio between the gap width and its midfrequency [42,43]

$$\Delta\omega \equiv \frac{\omega_{\mathrm{upper}} - \omega_{\mathrm{lower}}}{(\omega_{\mathrm{upper}} + \omega_{\mathrm{lower}})/2}, \tag{27}$$

where ω_{upper} and ω_{lower} denote the frequencies of upper and lower edges of the bandgap, respectively. Note that, when the quasi-steady and unsteady models are used to describe the aerodynamic loads generated by the flow, because of the damping ω_{upper} and ω_{lower} are defined as the upper and lower frequencies at which the attenuation constant is smaller than 1.0 percent. It has been previously shown that $\Delta\omega$ is an important design parameter and that a large relative size of the band gap is preferable for many applications [42,43].
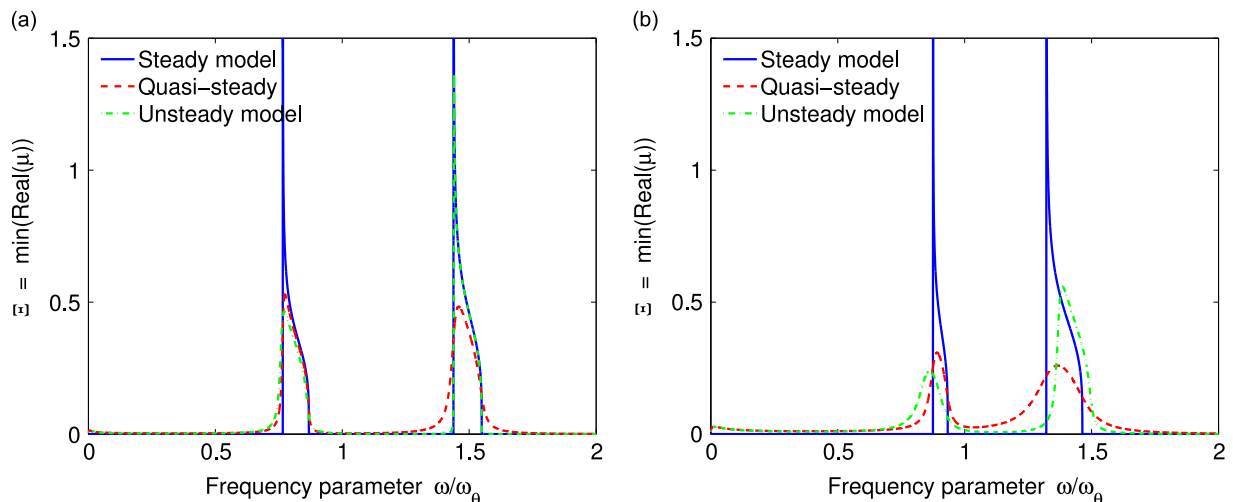

Fig. 6. Variation of the smallest attenuation constant $\Xi_{min} = \min(\mathrm{Real}(\mu_1))$ as a function of the frequency parameter ω/ω_θ for (a) $U=1$ and (b) $U=4$. Results obtained using all the three aerodynamic models introduced in Section 2 are shown.
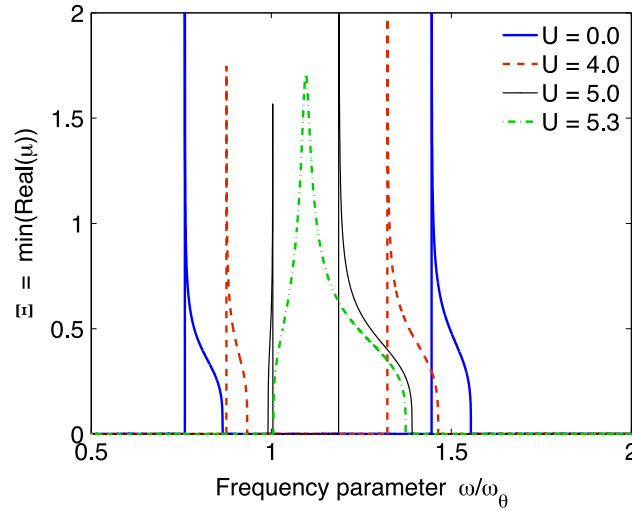
Fig. 7. Variation of the smallest attenuation constant $\Xi_{min} = \min(\mathrm{Real}(\mu))$ as a function of the frequency parameter ω/ω_θ for increasing values of the incident speed U.
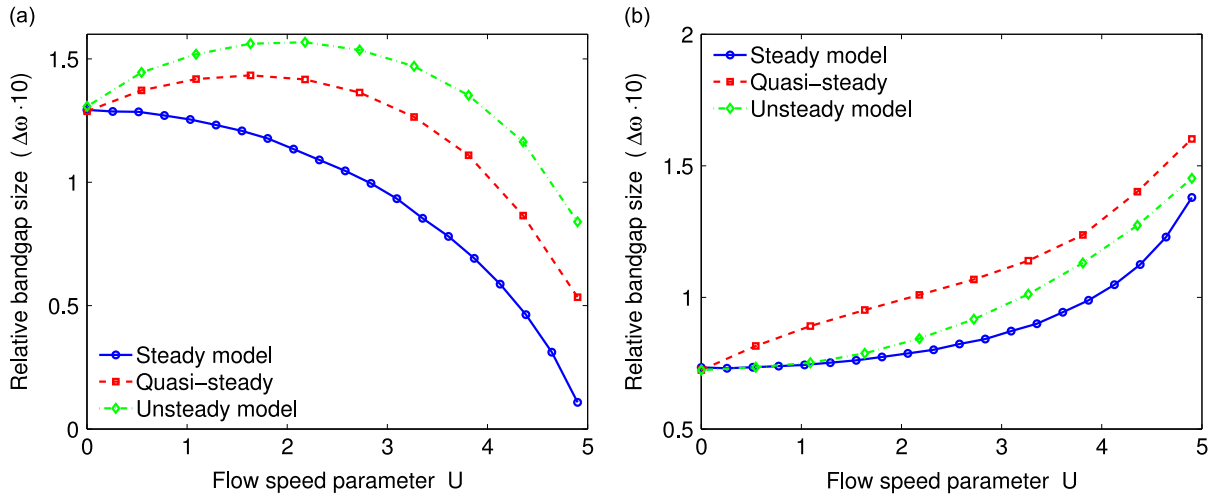

Fig. 8. Relative bandgap size $\Delta\omega$ associated to (a) bandgap #1 and (b) bandgap #2 as a function of the fluid speed U computed using the three aerodynamic models introduced in Section 2.

The dependence of $\Delta\omega$ on the flow speed U is shown in Fig. 8 for both bandgaps of the system. The results indicate that the size of the lower-frequency bandgap (bandgap #1) tends to decrease for increasing values of U, while the opposite trend is found for bandgap #2. This behavior is a direct consequence of the progressive convergence of the mid-frequency of two bandgaps which has the effect of increasing/decreasing the denominator of Eq. (27). This trend is further accentuated by the broadening of the plunge bandgap and the corresponding shrinking of the pitch gap as seen in Fig. 7. Fig. 8 also reveals that the relative bandgap size predicted by the quasi-steady and unsteady models is slightly larger than the one computed with steady aerodynamics. This is attributed to the broadening of the two bandgaps' width induced by the aerodynamic damping included in these models.

4.2.3. Effect of the system parameters on $\Delta\omega$

Having demonstrated through analytical calculations that the flow speed can be exploited to alter the bandgaps of our periodic system, we now proceed to investigate the effect of variations of the parameters defining its behavior on the relative bandgap size $\Delta\omega$. After extensive investigations, we found that the response of the system is mostly affected by the non-dimensional mass ratio ($\psi = M_{\mathrm{beam}}/m_a$), the inertia ratio ($r^2 = I_a/m_a b^2$) and the airfoil frequency ratio ($\sigma = \omega_h/\omega_\theta$). Therefore, we evaluated the effect of ψ, r^2 and σ, on $\Delta\omega$ for $U = 0$, 2 and 3. For the sake of simplicity, these calculations are conducted using the steady aerodynamic model which, despite its simplicity, has been shown to provide accurate predictions of the aeroelastic and wave propagation characteristic of the beam-airfoil system.

Effect of the mass ratio ψ: In Fig. 9 we show the effect of $\psi = M_{\text{beam}}/m_a$, which defines the amount of mass added to the beam by the resonating unit, on $\Delta\omega$. The results indicate that higher values of ψ (i.e. lower values of m_a) lead to significantly smaller bandgap sizes. This trend is expected, since it is well known that resonators with small mass result in less control authority on the primary system they act upon [44]. Fig. 9a also indicates that for the low-frequency gap induced by the pitch resonance (bandgap #1) this effect is exacerbated by the incident flow speed U, while the opposite trend is found in Fig. 9b for the high-frequency (plunge) gap (bandgap #2). This trends clearly correlate to the aeroelastic convergence of the two vibrational modes of the airfoils, which affect the central bandgap frequency and thus the denominator of Eq. (27).

Effect of the inertia ratio r^2: The inertia ratio r^2 is directly proportional to the mass polar moment of inertia I_a of the airfoil and is indicative of the mass distribution of the resonator along its chord-wise direction. Note that r^2 is also directly proportional to the pitch spring stiffness $k_\theta = \omega_h^2 I_a/\sigma^2$. Because of this, an increase of r^2 does not significantly affect the pitch natural frequency of the airfoil and consequently the mid-frequency of the associated bandgap. In fact, the results reported in Fig. 10a indicate that r^2 has a limited effect on $\Delta\omega$ associated with bandgap #1. An increase in r^2 slightly reduces the bandgap width (i.e. $\omega_{\text{upper}} - \omega_{\text{lower}}$) and therefore leads to a modest decrease of $\Delta\omega$.

An opposite trend is instead observed in Fig. 10b, indicating that the relative size of bandgap #2 (associated to the plunge mode) significantly increases with r^2. This behavior is mostly associated with a decrease of the midfrequency (i.e. $(\omega_{\text{upper}} + \omega_{\text{lower}})/2$) of this bandgap, which gradually approaches the first one. Therefore, also the flow speed required for a complete coalescence of the two gaps is found to decrease or increasing values of r^2, as confirmed by the results reported in Fig. 4b showing that higher values of r^2 tend to lower the flutter speed of the resonator.
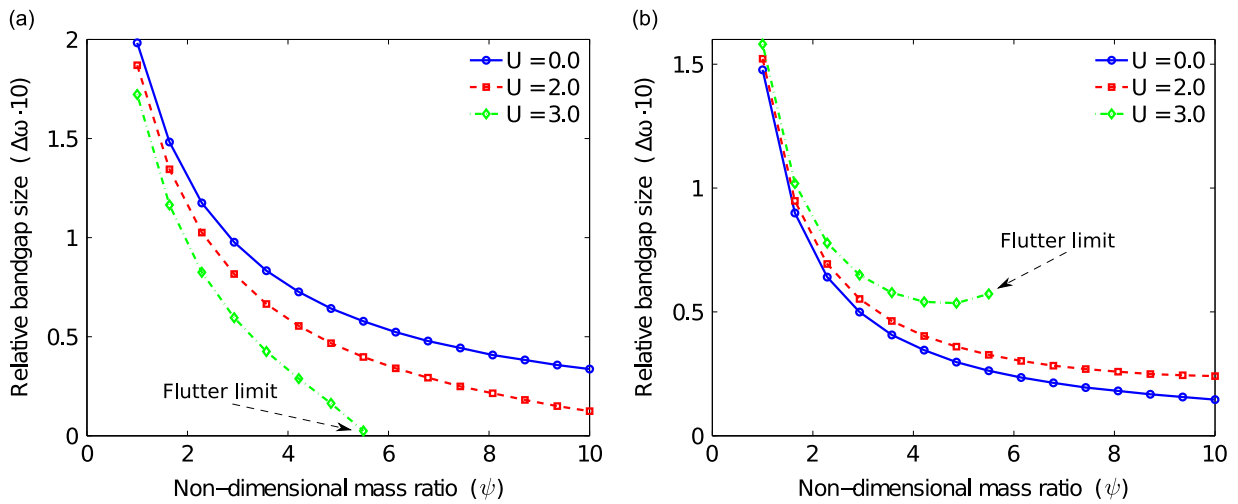

Fig. 9. Relative bandgap size $\Delta\omega$ associated to (a) bandgap #1 and (b) bandgap #2 as a function of the non-dimensional mass ratio ψ. The results are obtained using the steady aerodynamic model.
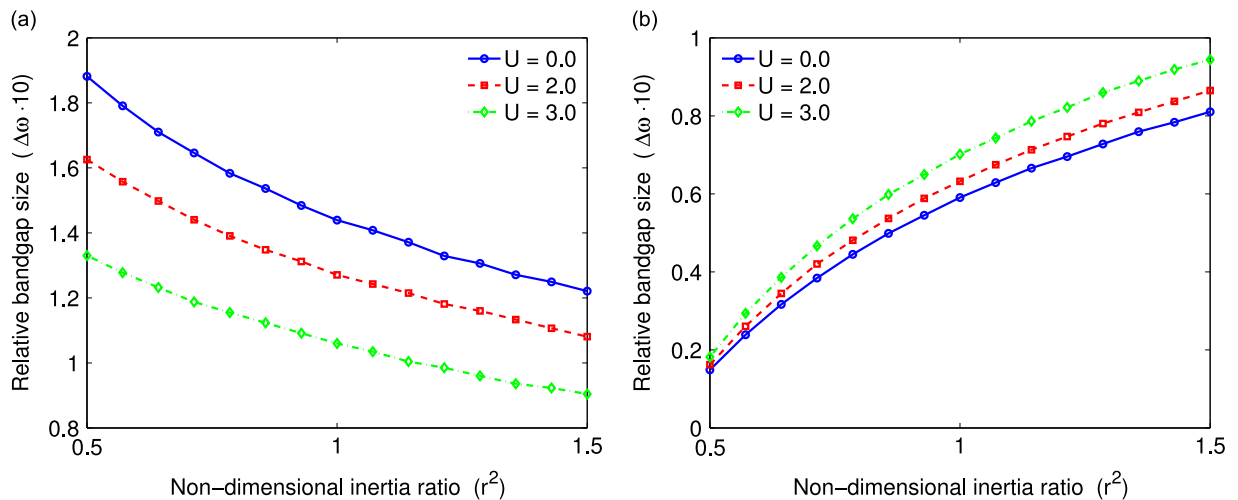

Fig. 10. Relative bandgap size $\Delta\omega$ associated to (a) bandgap #1 and (b) bandgap #2 as a function of the non-dimensional inertia ratio r^2. The results are obtained using the steady aerodynamic model.
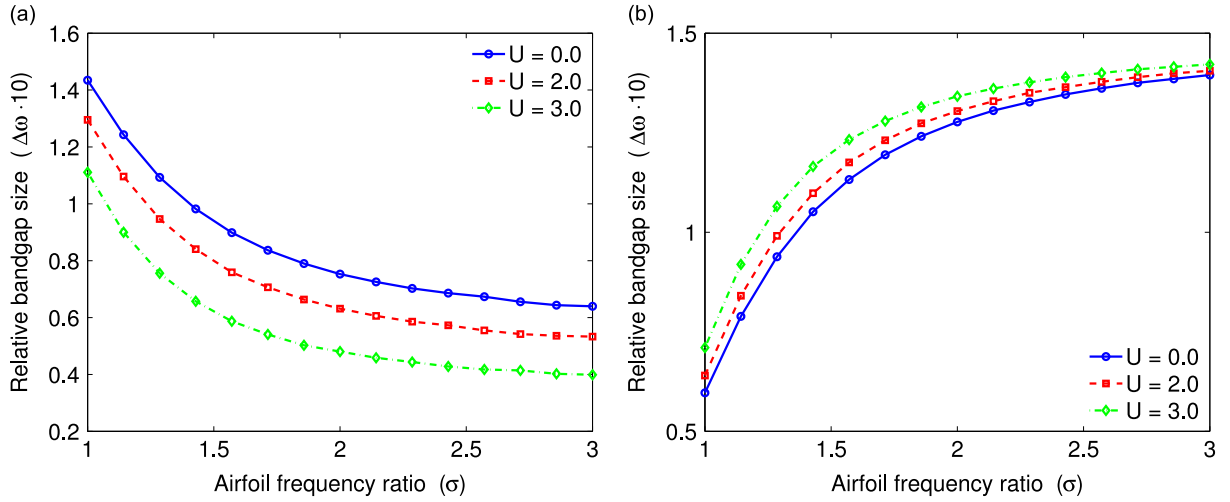
(a)

(b)

Fig. 11. Relative bandgap size $\Delta\omega$ associated to (a) bandgap #1 and (b) bandgap #2 as a function of the non-dimensional airfoil frequency ratio σ. The results are obtained using the steady aerodynamic model.

Effect of the airfoil frequency ratio σ: The airfoil frequency ratio $\sigma = \omega_h/\omega_\theta$ is defined as the ratio between the uncoupled natural frequencies of the airfoils at zero speed (i.e. $\omega_h = \sqrt{k_h/m_a}$, and $\omega_\theta = \sqrt{k_\theta/I_a}$), and is indicative of the frequency separation between the pitch and plunge resonances. Alternatively, the frequency parameter σ can also be interpreted as a ratio between the stiffness of the plunge (k_h) and pitch (k_θ) spring. Therefore, the results shown in Fig. 11a indicate that the size of the pitch bandgap (bandgap #1) decreases when the ratio between k_h and k_θ increases. The opposite trend is observed for $\Delta\omega$ associated with the plunge mode (see Fig. 11b), whose behavior is mostly dictated by the plunge spring with stiffness k_h.

5. Effective material description at long wavelengths

To further gain insights into the behavior of the system, we now obtain analytical expressions for the long-wavelength regime (i.e. $\kappa_b L \to 0$). These will enable us to obtain an equivalent beam model with effective mechanical properties which include the effects of the airfoil resonators.

Since the dynamic response of a unit cell comprising a beam and a fluid-coupled resonator attached to it is fully described by the dynamic system matrix $\mathbf{D}(\omega)$ (see Eqs. (21) and (22)), the long-wavelength behavior can be easily obtained by computing the limit of $\mathbf{D}(\omega)$ for $\kappa_b L \to 0$, namely

$$\lim_{\kappa_b L \to 0} \mathbf{D}(\omega) = \lim_{\kappa_b L \to 0} \begin{bmatrix} \mathbf{D}_{LL}(\omega) & \mathbf{D}_{LR}(\omega) \\ \mathbf{D}_{RL}(\omega) & \mathbf{D}_{RR}(\omega) \end{bmatrix}. \tag{28}$$

For the sake of simplicity, here we focus on the steady aerodynamic model for which a closed form solution of Eq. (28) can be obtained. For this case we find that the limit in Eq. (28) yields the static stiffness matrix of the beam, but with the bending stiffness EI replaced by an effective bending stiffness (EI*),

$$\text{EI}^*(\omega) = \text{EI} + \frac{L^3}{12} D_0(\omega), \tag{29}$$

which, interestingly, depends on the static bending stiffness of the beam (EI), and the fluid-coupled dynamic stiffness of the resonator (D_0) defined in Eq. (6). For example, the limit of $\mathbf{D}_{LL}$ in Eq. (28) yields

$$\lim_{\kappa_b L \to 0} \mathbf{D}_{LL} = \frac{\text{EI}^*(\omega)}{L^3} \begin{bmatrix} 12 & 6L \\ 6L & 4L^2 \end{bmatrix}. \tag{30}$$

The dependence of EI*/EI on the frequency parameter ω/ω_θ is presented in Fig. 12 for different values of the incident flow speed U. The resonant behavior of the vibration absorber is reflected in the equivalent mechanical behavior of the waveguide which exhibits peaks in the vicinity of the pitch and plunge resonance frequencies of the corresponding resonator. Interestingly, this behavior has also been observed in other internally resonating metamaterials and has been interpreted as the result of an apparent negative stiffness at the internal resonance [25].

The equivalent beam bending stiffness found through the derivations above is then used to estimate the equivalent dispersion properties of the waveguide. For a beam with equivalent bending stiffness EI* the wavenumber of flexural waves
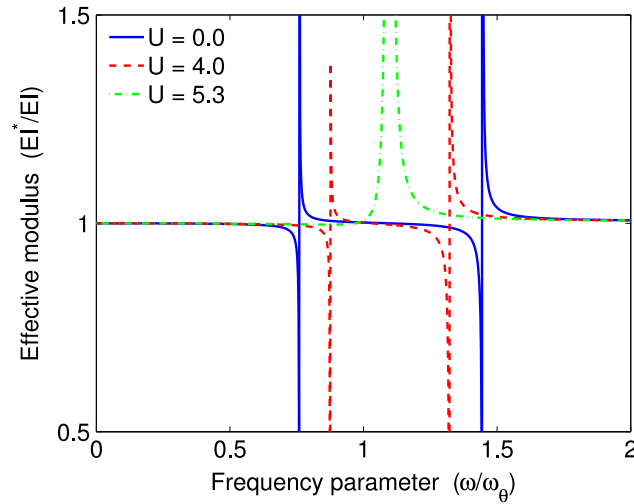
Fig. 12. Equivalent bending stiffness of the beam normalized with respect to its static value EI as a function of the frequency parameter ω/ω_θ.
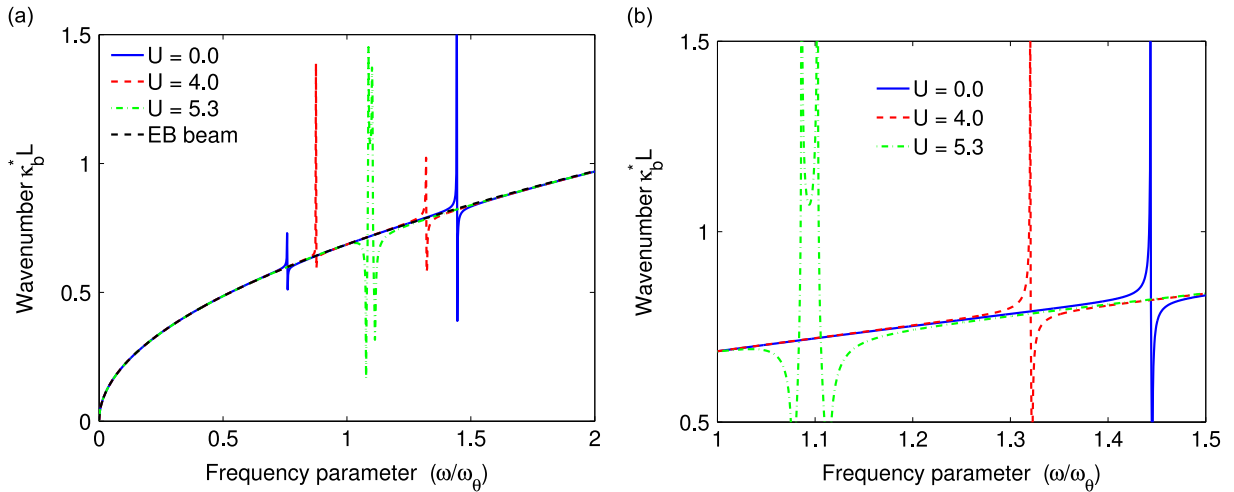

Fig. 13. (a) Analytical dispersion relations computed through the equivalent properties (Eq. (31)) for different values of flow speed U. (b) Details showing the variation of the high-frequency bandgap for increasing values of U.

is given by [45]

$$\kappa_b^*(\omega) = \left(\frac{m^*}{EI^*(\omega)} \omega^2 \right)^{1/4},$$

(31)

where the effective mass per unit length

$$m^* = m + m_a/L,$$

(32)

has been introduced (given by the sum of the mass per unit length of the beam (m) and mass of the flap divided by the length of the cell (m_a/L)). The dispersion relations computed through the equivalent properties in Eq. (31) are shown in Fig. 13. Interestingly, the results indicate that the equivalent properties' formulation developed herein is able to identify the attenuation bands induced by the pitch and plunge resonances of the airfoil, and their functional dependence on the speed of the incident fluid.

6. Conclusions

In this paper we investigate the propagation of waves in a beam with a periodic distribution airfoil-shaped resonating units (vibration absorbers). The system consists of a waveguide (beam) connected to a secondary system (airfoils) whose resonant behavior generates strong dispersion and wave attenuation characteristics. Furthermore, the airfoil-like shape of

the resonating masses enables the frequency ranges of wave attenuation (bandgaps) to be tuned by changes in the speed of the surrounding fluid.

The dispersion characteristics of the fluid-coupled waveguide are derived analytically through the transfer matrix approach, accounting explicitly for the aerodynamic coupling. Although both steady and unsteady aerodynamic models are used to describe the evolution of the aerodynamic loads acting on the resonating masses, the results indicate that, despite its simplicity, the steady-state aerodynamic model correctly captures the effect of the speed of the incident fluid on the bandgaps. Moreover, the influence of the most relevant parameters defining the system on the dispersion properties of the periodic beam is also evaluated.

Finally, further insights into the dynamic response of the waveguide is gained by determining its equivalent mechanical properties at long wavelengths. The effective bending stiffness confirms the locally resonant nature of the bandgaps and can be used to determine their dependence on the incident wind speed.

By harnessing fluid–structure interactions, we expand the capabilities of existing locally resonant metamaterials and design systems capable of sensing the surrounding fluid environment and change their response accordingly. This concept has the potential to dramatically impact a variety of applications, such as microfluidic devices, civil infrastructures, and defense systems. For example, the proposed system can lead to the design of sustainable and self-regulating vibration suppression devices capable of autonomously tracking and controlling the dynamic response of structures over a broad range of operative conditions.

Acknowledgments

Appendix A. Coefficients of Peter's unsteady model

According to Peters et al. [35], the evolution of the state vector $\lambda(t)$ containing the values of λ_n is given by (see Eq. (14) in the manuscript)

$$\mathbf{A}\dot{\lambda}(t) + \frac{V_\infty}{b}\lambda = \mathbf{c}\left[\ddot{h}(t) + V_\infty\dot{\theta}(t) + b\left(\frac{1}{2} - a\right)\ddot{\theta}(t)\right], \tag{A.1}$$

with the matrix $\mathbf{A}$ given by

$$\mathbf{A} = \mathbf{D} + \boldsymbol{d}^T\mathbf{b} + \mathbf{c}^T\boldsymbol{d} + \tfrac{1}{2}\mathbf{c}^T\mathbf{b}. \tag{A.2}$$

while matrix $\mathbf{D}$ and vectors $\mathbf{b}$, $\mathbf{c}$, and $\boldsymbol{d}$ depend on the number of induced flow states N_p and are defined as

$$D_{ij} = \begin{cases} \dfrac{1}{2i} & \text{for } i = j+1 \\[2mm] -\dfrac{1}{2i} & \text{for } i = j-1 \\[2mm] 0 & \text{for } i \neq j \pm 1 \end{cases}$$

$$b_i = \begin{cases} (-1)^{i-1}\dfrac{(N_p+i-1)!}{(N_p-i-1)!} \cdot \dfrac{1}{(i!)^2} & \text{for } i \neq N_p \\[2mm] (-1)^{i-1} & \text{for } i = N_p \end{cases}$$

$$d_i = \begin{cases} \dfrac{1}{2} & \text{for } i = 1 \\[2mm] 0 & \text{for } i \neq 1 \end{cases}$$

$$c_i = \frac{2}{i} \tag{A.3}$$

Appendix B. Comparison between analytical and FE dispersion relations

In Fig. B1 we compare the dispersion relations computed analytically and through FE calculations using the quasi-steady and unsteady aerodynamic models. Excellent agreement between the two sets of results is found, validating the implementation of both methods.
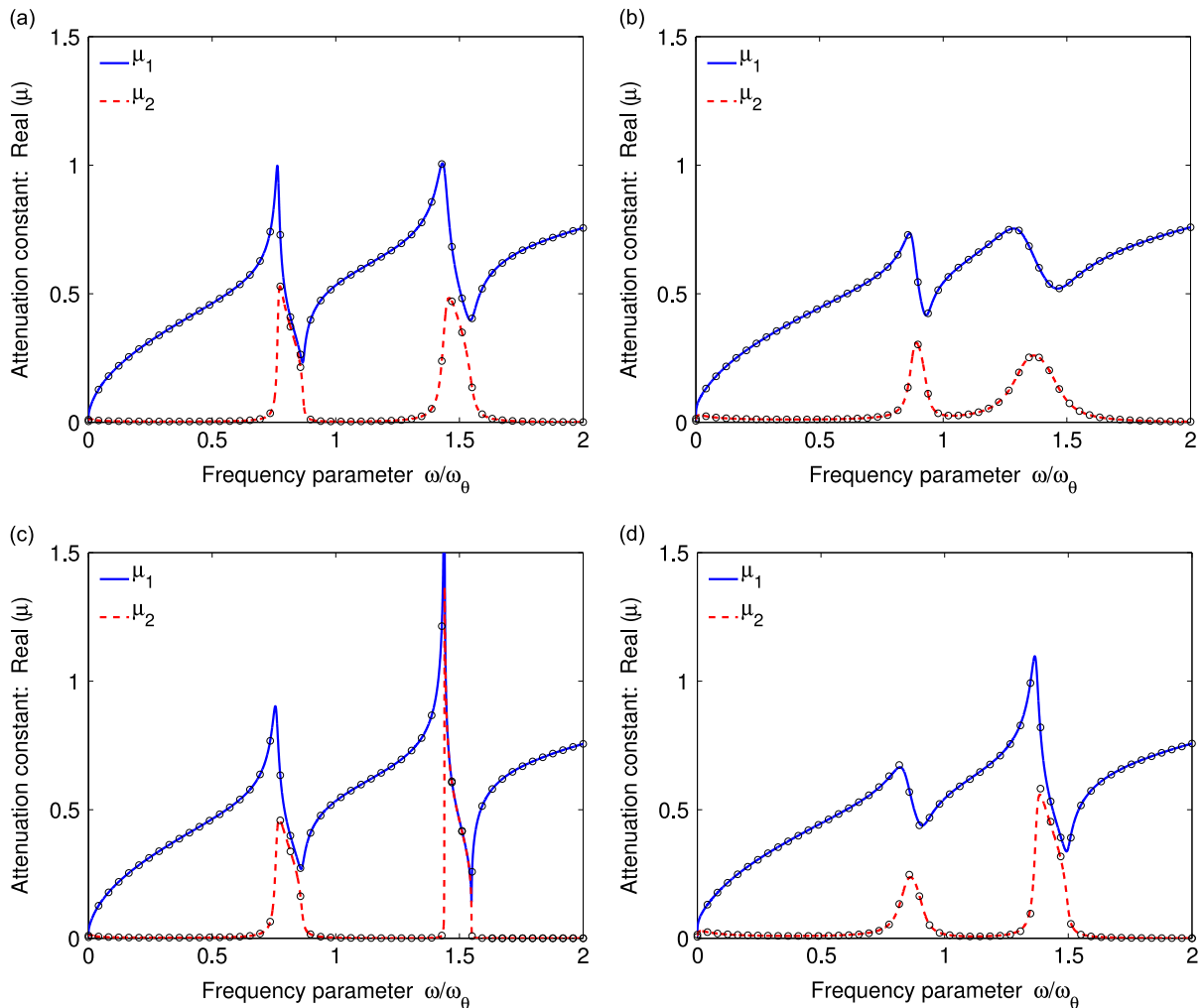
Fig. B1. Attenuation constants associated with μ_1 (solid blue line), and μ_2 (dashed red line) computed using the (a, b) quasi-steady and (c, d) unsteady aerodynamic models for different values of the incident flow speed. Excellent agreement is found between the analytical (lines) and corresponding FE (○ markers) results. (a) Quasi-steady model ($U=1.0$). (b) Quasi-steady model ($U=4.0$). (c) Unsteady model ($U=1.0$). (d) Unsteady model ($U=4.0$). (For interpretation of the references to color in this figure caption, the reader is referred to the web version of this paper.)

References

[1] D.J. Mead, Wave propagation in continuous periodic structures: research contributions from Southampton, 1964–1995, *Journal of Sound and Vibration* 190 (3) (1996) 495–524.
[2] M. Sigalas, E. Economou, Band structure of elastic waves in two dimensional systems, *Solid State Communications* 86 (3) (1993) 141–143.
[3] R. Martinezsala, J. Sancho, J. Sanchez, V. Gómez, J. Llinares, F. Meseguer, Sound-attenuation by sculpture, *Nature* 378 (6554) (1995) 241.
[4] W. Cheng, J. Wang, U. Jonas, G. Fytas, N. Stefanou, Observation and tuning of hypersonic bandgaps in colloidal crystals, *Nature Materials* 5 (10) (2006) 830–836.
[5] Z. Liu, X. Zhang, Y. Mao, Y. Zhu, Z. Yang, C. Chan, P. Sheng, Locally resonant sonic materials, *Science* 289 (5485) (2000) 1734–1736.
[6] N. Fang, D. Xi, J. Xu, M. Ambati, W. Srituravanich, C. Sun, X. Zhang, Ultrasonic metamaterials with negative modulus, *Nature Materials* 5 (6) (2006) 452–456.
[7] L. Airoldi, M. Ruzzene, Design of tunable acoustic metamaterials through periodic arrays of resonant shunted piezos, *New Journal of Physics* 13 (11) (2011) 113010.
[8] M. Sigalas, E. Economou, Elastic and acoustic wave band structure, *Journal of Sound and Vibration* 158 (2) (1992) 377–382.
[9] K.M. Ho, C.K. Cheng, Z. Yang, X. Zhang, P. Sheng, Broadband locally resonant sonic shields, *Applied Physics Letters* 83 (26) (2003) 5566–5568.
[10] Z. Yang, H. Dai, N. Chan, G. Ma, P. Sheng, Acoustic metamaterial panels for sound attenuation in the 50–1000 Hz regime, *Applied Physics Letters* 96 (4) (2010) 041906.
[11] F. Casadei, B. Beck, K. Cunefare, M. Ruzzene, Vibration control of through hybrid configurations of periodic piezoelectric shunts, *Journal of Intelligent Material Systems and Structures* 23 (10) (2012) 1169–1177.
[12] F. Casadei, L. Dozio, M. Ruzzene, K. Cunefare, Periodic shunted arrays for the control of noise radiation in an enclosure, *Journal of Sound and Vibration* 329 (18) (2010) 3632–3646.
[13] Y. Xiao, J. Wen, X. Wen, Sound transmission loss of metamaterial-based thin plates with multiple subwavelength arrays of attached resonators, *Journal of Sound and Vibration* 331 (25) (2012) 5408–5423.

[14] F. Tateo, M. Collet, B. Beck, K. Cunefare, Vibration control of plates through a periodic array of shunted piezoelectric patches with negative capacitance circuits, in: SPIE Smart Structures and Materials+ Nondestructive Evaluation and Health Monitoring, International Society for Optics and Photonics, 2014.
[15] G. Wang, X. Wen, J. Wen, Y. Liu, Quasi-one-dimensional periodic structure with locally resonant band gap, *Journal of Applied Mechanics* 73 (1) (2006) 167–170.
[16] Y. Song, J. Wen, D. Yu, X. Wen, Analysis and enhancement of torsional vibration stopbands in a periodic shaft system, *Journal of Physics D: Applied Physics* 46 (14) (2013) 145306.
[17] D. Yu, Y. Liu, G. Wang, H. Zhao, J. Qiu, Flexural vibration band gaps in Timoshenko beams with locally resonant structures, *Journal of Applied Physics* 100 (12) (2006) 124901.
[18] Y. Xiao, J. Wen, D. Yu, X. Wen, Flexural wave propagation in beams with periodically attached vibration absorbers: band-gap behavior and band formation mechanisms, *Journal of Sound and Vibration* 332 (4) (2012) 867–893.
[19] L. Raghavan, A.S. Phani, Local resonance bandgaps in periodic media: theory and experiment, *The Journal of the Acoustical Society of America* 134 (2013) 1950.
[20] O. Thorp, M. Ruzzene, A. Baz, Attenuation of wave propagation in fluid-loaded shells with periodic shunted piezoelectric rings, *Smart Materials and Structures* 14 (4) (2005) 594.
[21] M. Oudich, M. Senesi, M.B. Assouar, M. Ruzenne, J.-H. Sun, B. Vincent, Z. Hou, T.-T. Wu, Experimental evidence of locally resonant sonic band gap in two-dimensional phononic stubbed plates, *Physical Review B* 84 (16) (2011) 165136.
[22] C.-Y. Sun, J.-C. Hsu, T.-T. Wu, Resonant slow modes in phononic crystal with periodic membranes, *Applied Physics Letters* 97 (3) (2010) 031902.
[23] B.S. Lazarov, J.S. Jensen, Low-frequency band gaps in chains with attached non-linear oscillators, *International Journal of Non-Linear Mechanics* 42 (10) (2007) 1186–1193.
[24] S. Yao, X. Zhou, G. Hu, Experimental study on negative effective mass in a 1d mass–spring system, *New Journal of Physics* 10 (4) (2008) 043020.
[25] H. Huang, C. Sun, G. Huang, On the negative effective mass density in acoustic metamaterials, *International Journal of Engineering Science* 47 (4) (2009) 610–617.
[26] Y. Xiao, J. Wen, X. Wen, Longitudinal wave band gaps in metamaterial-based elastic rods containing multi-degree-of-freedom resonators, *New Journal of Physics* 14 (3) (2012) 033042.
[27] G. Huang, C. Sun, Band gaps in a multiresonator acoustic metamaterial, *Transactions of the ASME-L-Journal of Vibration and Acoustics* 132 (3) (2010) 031003.
[28] P.F. Pai, Metamaterial-based broadband elastic wave absorber, *Journal of Intelligent Material Systems and Structures* 21 (5) (2010) 517–528.
[29] P. Celli, S. Gonella, Laser-enabled experimental wavefield reconstruction in two-dimensional phononic crystals, *Journal of Sound and Vibration* 333 (1) (2014) 114–123.
[30] A. Spadoni, M. Ruzzene, K. Cunefare, Vibration and wave propagation control of plates with periodic arrays of shunted piezoelectric patches, *Journal of Intelligent Material Systems and Structures* 20 (8) (2009) 979–990.
[31] F. Casadei, T. Delpero, A. Bergamini, P. Ermanni, M. Ruzzene, Piezoelectric resonator arrays for tunable acoustic waveguides and metamaterials, *Journal of Applied Physics* 112 (6) (2012) 064902.
[32] F. Casadei, K. Bertoldi, Harnessing fluid–structure interactions to design self-regulating acoustic metamaterials, *Journal of Applied Physics* 115 (3) (2014) 034907–034913.
[33] A. Collar, The first fifty years of aeroelasticity, *Aerospace* 5 (2) (1978) 12–20.
[34] D. Hodges, G. Pierce, *Introduction to Structural Dynamics and Aeroelasticity*, vol. 15, Cambridge University Press, Cambridge, United Kingdom, 2011.
[35] D.A. Peters, S. Karunamoorthy, W.-M. Cao, Finite state induced flow models. I: two-dimensional thin airfoil, *Journal of Aircraft* 32 (2) (1995) 313–322.
[36] J.F. Doyle, *Wave Propagation in Structures*, Springer, New York, 1989.
[37] Y.-K. Lin, T. McDaniel, Dynamics of beam-type periodic structures, *Journal of Engineering for Industry* 91 (1969) 1133.
[38] F. Bloch, Über die quantenmechanik der elektronen in kristallgittern, *Zeitschrift für physik* 52 (7–8) (1929) 555–600.
[39] L. Brillouin, *Wave Propagation in Periodic Structures: Electric Filters and Crystal Lattices*, Courier Dover Publications, Mineola, New York, 2003.
[40] I. Garrick, W.H. Reed III, Historical development of aircraft flutter, *Journal of Aircraft* 18 (11) (1981) 897–912.
[41] F. Casadei, M. Ruzzene, L. Dozio, K. Cunefare, Broadband vibration control through periodic arrays of resonant shunts: experimental investigation on plates, *Smart Materials and Structures* 19 (1) (2009) 015002.
[42] M. Maldovan, E. Thomas, Simultaneous complete elastic and electromagnetic band gaps in periodic structures, *Applied Physics B* 83 (4) (2006) 595–600.
[43] P. Wang, J. Shim, K. Bertoldi, Effects of geometric and material nonlinearities on tunable band gaps and low-frequency directionality of phononic crystals, *Physical Review B* 88 (1) (2013) 014304.
[44] J.P. den Hartog, *Mechanical Vibrations*, DoverPublications.com, New York, 1956.
[45] J. Achenbach, *Wave Propagation in Elastic Solids*, Access Online via Elsevier, North-Holland Publishing Company, Amsterdam, 1984.
[46] P. Wang, F. Casadei, S. Shan, J.C. Weaver, K. Bertoldi, Harnessing buckling to design tunable locally resonant acoustic metamaterials, *Physical Review Letters* 113 (2014) 014301.